Improved Infrared Photometry and a Preliminary Parallax Measurement for the Extremely Cold Brown Dwarf CWISEP J144606.62-231717.8

Federico Marocco[1,2,8] , J. Davy Kirkpatrick[2] , Aaron M. Meisner[3] , Dan Caselden[4] , Peter R. M. Eisenhardt[1],
Michael C. Cushing[5] , Jacqueline K. Faherty[6] , Christopher R. Gelino[2], and Edward L. Wright[7]

[1] Jet Propulsion Laboratory, California Institute of Technology, 4800 Oak Grove Drive, Pasadena, CA 91109, USA; federico.marocco@jpl.nasa.gov
[2] IPAC, Mail Code 100-22, Caltech, 1200 E. California Boulevard, Pasadena, CA 91125, USA
[3] NSF's National Optical-Infrared Astronomy Research Laboratory, 950 North Cherry Avenue, Tucson, AZ 85719, USA
[4] Gigamon Applied Threat Research, 619 Western Avenue, Suite 200, Seattle, WA 98104, USA
[5] Department of Physics and Astronomy, University of Toledo, 2801 West Bancroft Street, Toledo, OH 43606, USA
[6] Department of Astrophysics, American Museum of Natural History, Central Park West at 79th Street, NY 10024, USA
[7] Department of Physics and Astronomy, UCLA, 430 Portola Plaza, Box 951547, Los Angeles, CA 90095-1547, USA

Abstract

We present follow-up *Spitzer* observations at 3.6 μm (ch1) and 4.5 μm (ch2) of CWISEP J144606.62–231717.8, one of the coldest known brown dwarfs in the solar neighborhood. This object was found by mining the *Wide-field Infrared Survey Explorer* (*WISE*) and NEOWISE data via the CatWISE Preliminary Catalog by Meisner et al., where an initial *Spitzer* color of ch1–ch2 = 3.71 ± 0.44 mag was reported, implying it could be one of the reddest, and hence coldest, known brown dwarfs. Additional *Spitzer* data presented here allows us to revise its color to ch1–ch2 = 2.986 ± 0.048 mag, which makes CWISEP J144606.62–231717.8 the fifth reddest brown dwarf ever observed. A preliminary trigonometric parallax measurement, based on a combination of *WISE* and *Spitzer* astrometry, places this object at a distance of $10.1^{+1.7}_{-1.3}$ pc. Based on our improved *Spitzer* color and preliminary parallax, CWISEP J144606.62–231717.8 has a $T_{\rm eff}$ in the 310–360 K range. Assuming an age of 0.5–13 Gyr, this corresponds to a mass between 2 and 20 $M_{\rm Jup}$.

Unified Astronomy Thesaurus concepts: Brown dwarfs (185); Y dwarfs (1827); Solar neighborhood (1509); Trigonometric parallax (1713); Proper motions (1295)

1. Introduction

Discovered in *Wide-field Infrared Survey Explorer* (*WISE*) data in 2014, WISE J085510.83–071442.5 (Luhman 2014, hereafter W0855) remains the coldest brown dwarf known. With an estimated effective temperature of ~250 K, W0855 represents an isolated extreme of the substellar spectral sequence. However, the census of the coldest, lowest-mass constituents of the solar neighborhood is known to be incomplete. Kirkpatrick et al. (2019) have estimated the current completeness limit to be 19 pc in the 900–1050 K interval, but to decrease to only 8 pc in the 300–450 K interval. At even lower $T_{\rm eff}$, W0855 is the only object known.

Obtaining a more complete census of extremely cold brown dwarfs is a fundamental step toward robustly constraining the efficiency and history of the star formation process at its lowest mass (Kirkpatrick et al. 2019). Solivagant objects with mass as low as a few Jupiter masses ($M_{\rm Jup}$) have been found in star formation regions and nearby, young moving groups (Faherty et al. 2016; Zapatero Osorio et al. 2017; Luhman et al. 2018; Lodieu et al. 2018; Esplin & Luhman 2019). Older, isolated objects with these masses therefore should exist, and numerical simulations show that their space density is extremely sensitive to the low-mass cutoff for star formation (Kirkpatrick et al. 2019).

Using data from the recently released CatWISE Preliminary Catalog (Eisenhardt et al. 2019) and a combination of machine-learning and color-, magnitude-, and proper motion-based selection criteria, Meisner et al. (2019a, hereafter M19) identified a large sample of candidate cool brown dwarfs in

the solar neighborhood. Through a dedicated *Spitzer* observing campaign to obtain 3.6 μm (ch1) and 4.5 μm (ch2) data and improved proper motion measurement, M19 confirmed 114 objects in their sample to be nearby brown dwarfs, with 17 of them having *Spitzer* ch1–ch2 color clearly indicating $T_{\rm eff} < 460$ K, corresponding to spectral type Y0 or later. CWISEP J144606.62–231717.8 (hereafter CW1446) stands out among them, with a ch1–ch2 color of 3.71 ± 0.44 mag, potentially supplanting W0855 (ch1–ch2 = 3.55 ± 0.07 mag) as the reddest and therefore coldest brown dwarf known. Here we present additional *Spitzer* observations that better constrain the color of this source, and provide a preliminary measurement of its parallax.

In Section 2, we briefly summarize the brown dwarf candidate selection that led to the discovery of CW1446 and the data available prior to this Letter. In Section 3 we present new *Spitzer* follow-up observations and the resulting improved photometry, and in Section 4 we combine all of the *Spitzer* and *WISE* astrometry to obtain a preliminary parallax measurement. In Section 5 we derive the basic properties for CW1446, and in Section 6 we put this new object into context and discuss future work.

2. Source Selection and Existing Data

CW1446 was found as part of our larger effort to complete the census of very cold brown dwarfs in the solar neighborhood using the CatWISE Preliminary Catalog,[9] an infrared photometric and astrometric catalog consisting of 900,849,014

---

[8] NASA Postdoctoral Program Fellow.

[9] Available at https://irsa.ipac.caltech.edu/cgi-bin/Gator/nph-scan?mission=irsa&submit=Select&projshort=WISE and catwise.github.io.

Table 1
Photometry and Astrometry for CW1446

Parameter	Units	Value	Ref.	Notes
FLAMINGOS-2 J	mag	>22.36	M19	
CatWISE $W1$	mag	18.281 ± 0.292	M19	motion fit
CatWISE $W2$	mag	15.998 ± 0.094	M19	motion fit
Spitzer ch1	mag	19.682 ± 0.424	M19	aperture–2019 May
Spitzer ch2	mag	15.915 ± 0.022	M19	aperture–2019 May
Spitzer ch1	mag	19.340 ± 0.445	M19	PRF fit–2019 May
Spitzer ch2	mag	15.689 ± 0.026	M19	PRF fit–2019 May
Spitzer ch1	mag	18.951 ± 0.034	this Letter	aperture–2019 Nov
Spitzer ch2	mag	15.927 ± 0.017	this Letter	aperture–2019 Nov
Spitzer ch1	mag	18.905 ± 0.045	this Letter	PRF fit–2019 Nov
Spitzer ch2	mag	15.919 ± 0.018	this Letter	PRF fit–2019 Nov
ϖ	mas	99.2 ± 14.7	this Letter	
$\mu_\alpha \cos \delta$	mas yr^{-1}	-794.3 ± 51.9	this Letter	
μ_δ	mas yr^{-1}	-964.8 ± 30.7	this Letter	
$v_{\rm tan}$	km s^{-1}	59.7 ± 9.0	this Letter	

sources over the entire sky selected from *WISE* and NEOWISE data collected from 2010 to 2016 at *W1* (3.4 μm) and *W2* (4.6 μm; Eisenhardt et al. 2019).

The search was conducted using the PYTHON package XGBoost[10] (Chen & Guestrin 2016), which implements machine-learning algorithms under the gradient boosting framework. A detailed description of the search procedure is given in Marocco et al. (2019), and here we only briefly summarize the most important steps.

We trained the XGBoost model with a set of known T and Y dwarfs taken from the literature, cross-matched against CatWISE to obtain their CatWISE data. The model was trained on a set of the CatWISE data available for a given source, including aperture and point-spread function (PSF) photometry, proper motion, the χ^2 of the measurements, and artifact flags. Sample weights were applied to mitigate the class imbalance in the training set.

After training the XGBoost classifier with our initial training set, we applied it to the entire CatWISE catalog, and selected ~10,000 objects with the highest predicted probability of being cold brown dwarfs. We then visually inspected each object, using available optical, near- and mid-infrared images and the online image blinking/visualization tool WiseView[11] (Caselden et al. 2018). Objects passing this inspection, with *W1*–*W2* color visually consistent with *W1*–*W2* > 1 mag, and with by-eye motion,[12] were added to the training set. We then iterated by re-training the classifier on the full training data, and applied the re-trained classifier to the entire catalog to select another batch of high-probability positive class entries. The selection yielded an initial sample of 32 late-T and Y dwarf candidates, with either no detection or a marginal detection in *W1* and visible motion. These were followed up through our *Spitzer* campaign (program 14034, PI: A. M. Meisner) to obtain ch1 and ch2 photometry to estimate effective temperature and photometric distance. The results are presented in M19. CW1446 is the reddest (therefore the coldest) among the objects presented in M19, with ch2 = 15.802 ± 0.024 mag, and ch1–ch2 = 3.71 ± 0.44 mag. Photometric data available prior to our follow-up is summarized in Table 1.

3. *Spitzer* Follow-up

Follow-up *Spitzer* ch1 observations were taken as part of program 14307 (PI: F. Marocco). We took 36 exposures of 100 s, using a random dither pattern of medium scale. The total integration time was designed to achieve a signal-to-noise ratio (S/N) ~ 10, based on the ch1 magnitude from our PID 14034 data. Photometry was measured following the same procedure described in Marocco et al. (2019). The new ch1 mosaic is presented in Figure 1.

We also obtained *Spitzer* ch2 photometry as part of program 14224 (PI: J. D. Kirkpatrick). Because these observations were intended for high-precision astrometry, we designed the observations to have S/N > 100 at each epoch. Given the brightness of CW1446 (*W2* ~ 15.8 mag), we took nine exposures of 100 s using a random dither pattern of medium scale.
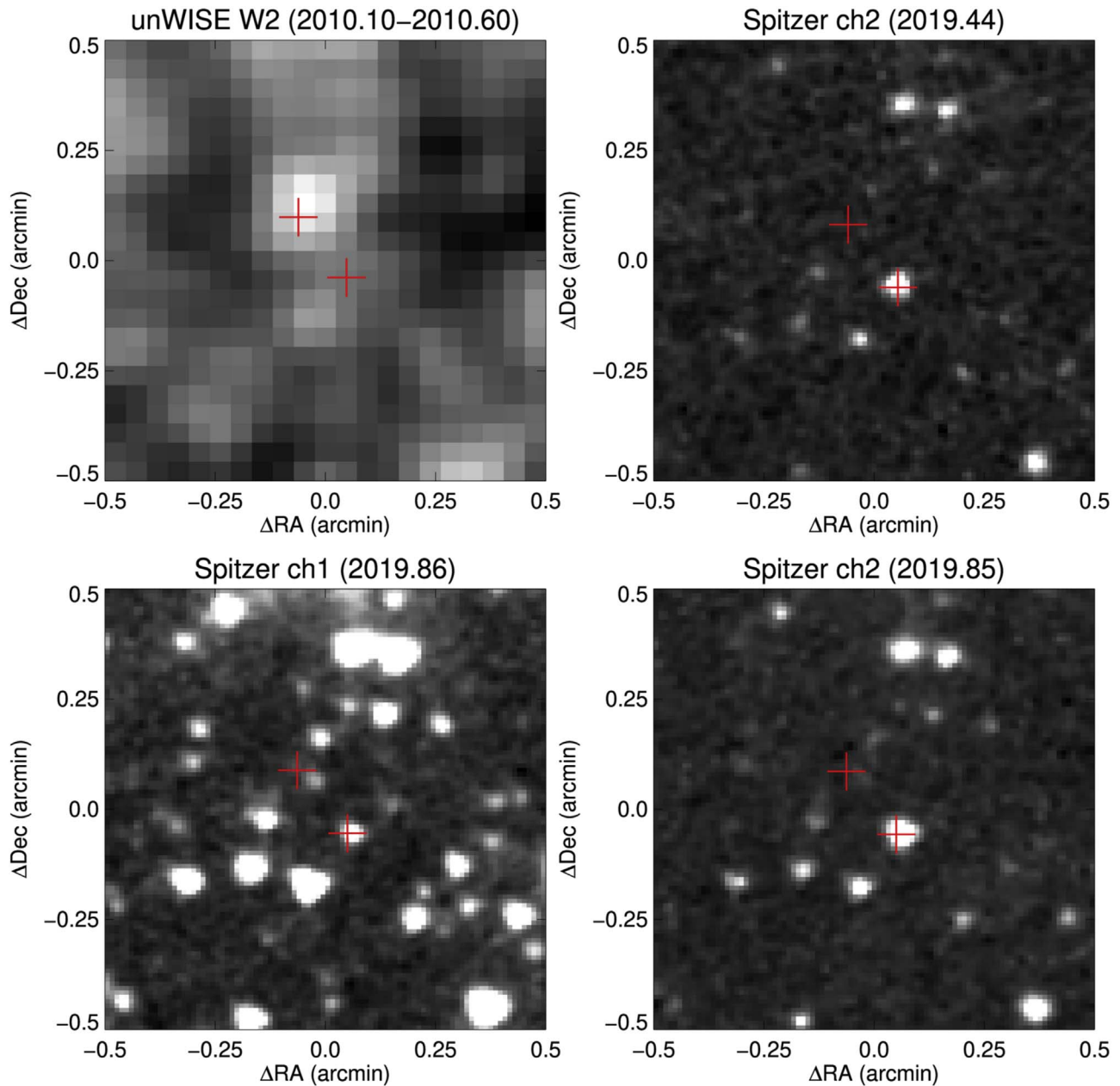
We performed both aperture and point response function (PRF)-fit photometric measurements using using the *Spitzer* MOsaicker and Point Source EXtractor with point-source extraction package (MOPEX/APEX; Makovoz & Khan 2005; Makovoz & Marleau 2005). Custom mosaics were built to provide better cosmic-ray removal than the default post basic calibrated data files provide. For this custom processing we coadded the corrected basic calibrated data (CBCD) frames and ran detections on the resultant coadd. Raw fluxes were then measured by MOPEX/APEX using the stack of individual CBCD files that comprised the coadd. These raw fluxes were converted to magnitudes by applying aperture corrections and comparing to the published ch1 and ch2 flux zero-points, as described in Section 5.1 of Kirkpatrick et al. (2019).

The new ch1 and ch2 measurements, presented in Table 1, yield a revised ch1–ch2 color of 2.986 ± 0.048 mag (PRF; the aperture color is 3.024 ± 0.038 mag). The new color is significantly bluer than its preliminary value (3.71 ± 0.44 mag), mostly because of the large difference in ch1. The measured ch1 PRF flux from the early *Spitzer* observations is 5.3 ± 2.1 μJy, while the new measurement is 7.86 ± 0.31 μJy, corresponding to a 1.2σ difference, while the aperture flux measurements are 3.1 ± 1.2 μJy and 6.11 ± 0.18 μJy, respectively, corresponding to a 2.5σ difference.

---

[10] https://xgboost.readthedocs.io/en/latest/
[11] http://byw.tools/wiseview
[12] Roughly $\frac{1}{2}$ pixel over the 8-years baseline, or $\approx$170 mas yr^{-1}.

Figure 1. 1 × 1 arcmin cutouts from the unWISE *W2* epoch coadd (top-left panel; Meisner et al. 2019b), and the *Spitzer* ch1 and ch2 mosaics, centered around CW1446. Red crosses mark its position at the earliest unWISE epoch (2010.10–2010.60), and the first *Spitzer* epoch (2019.44). The second *Spitzer* epoch exhibits motion along the R.A. axis, which is not consistent with the proper motion of the source, hinting at its large parallactic motion (see Section 4 for details).

4. Astrometry

Kirkpatrick et al. (2019) describes the methodology used to measure astrometry from the *Spitzer* images, but we have made a few improvements since then. First, we now match bright re-registration stars in each frame to *Gaia* data release 2 (DR2) and use only those *Gaia* stars that have full five-parameter solutions. Second, in order to assure that we have enough stars per frame with which to do the re-registration, we select stars down to a S/N value of 30. For CW1446, this resulted in 56 re-registration stars. Third, because we have chosen re-registration stars with full astrometric solutions, we can predict their absolute positions at the time of each *Spitzer* epochal observation, thus allowing us to measure astrometry on the absolute reference frame from the start. Therefore, no relative-to-absolute adjustment is needed.

The original *Spitzer* ch2 observation from program 14034 (PI: A. M. Meisner) was the only one obtained in the penultimate observing window. We have requested six additional ch2 observations in the final *Spitzer* observing window, which was open from 2019 early-November through mid-December. We present the first of those six observations here. These *Spitzer* data alone, however, are not sufficient to decouple proper motion and parallax. For this we relied on *WISE W2* detections. Specifically, we took the 12 unWISE epochal coadds (Meisner et al. 2019b, and references therein) spanning the range 2010 February–2018 July, and performed CROWDSOURCE (Schlafly et al. 2019, 2018) detections on the full unWISE tile containing the position of CW1446 (tile 2215m228, centered on R.A. = 221°5, decl. = −22°8). For each epoch, we matched these detections to objects in
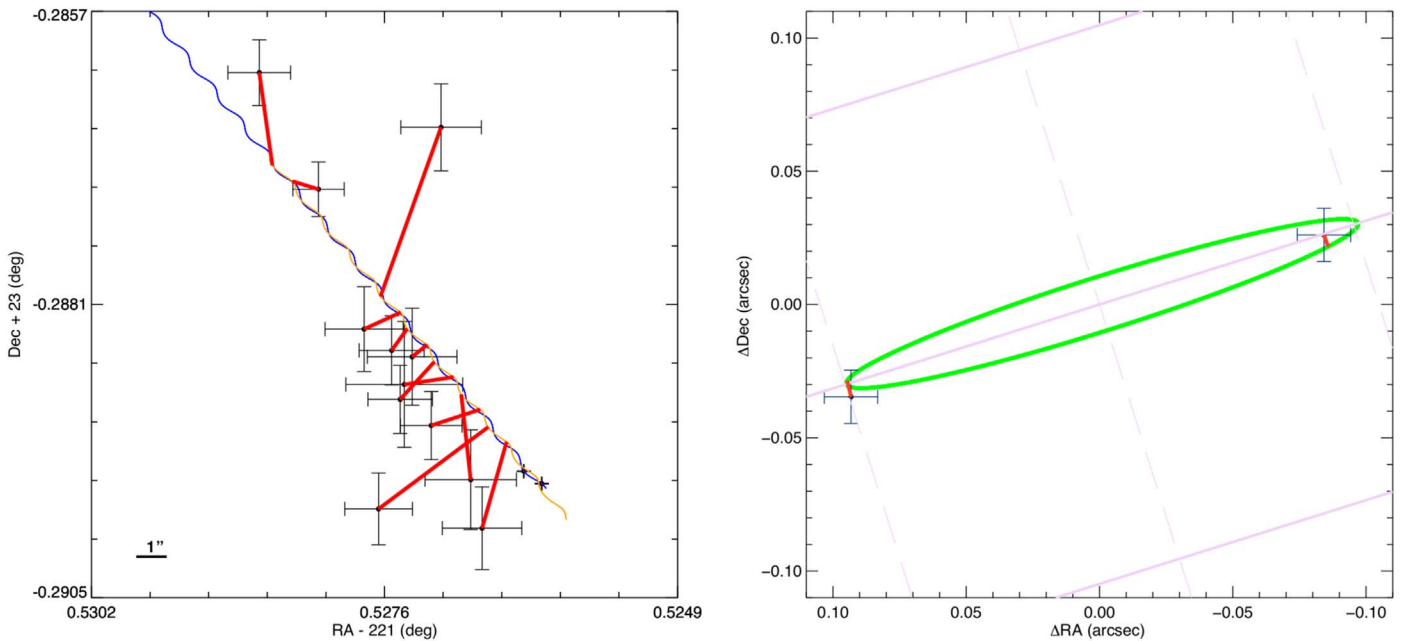
Figure 2. Proper motion + parallax fit to the combined *Spitzer* and unWISE *W2* data for CW1446. Left panels: the full astrometric solution and full set of empirical measurements. The unWISE *W2* epochal data are shown by the black points with large error bars and the *Spitzer* data are shown by the the black points with the much smaller error bars. The fit of the astrometric path of the object as seen from *Spitzer* is shown by the blue curve, and the astrometric path as seen from the Earth is shown by the orange curve. The red lines connect each data point with the spot on the relevant curve at that epoch. Right panels: a square patch of sky centered at the mean equatorial position of the target. The green curve is the parallactic fit, which is just the blue curve in the previous panel with the proper motion vector removed. The solid and dashed pale purple lines are the ecliptic latitude and longitude coordinate grid, respectively. This panel omits, for clarity, the less accurate unWISE astrometry.
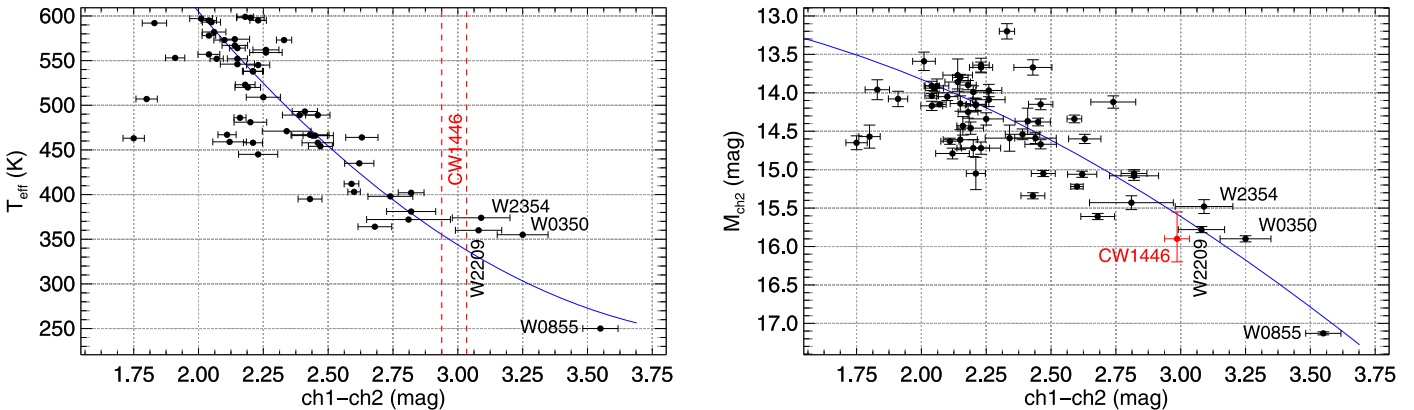
Figure 3. $T_{\rm eff}$ (left panel) and absolute *Spitzer* ch2 magnitude (right panel) as a function of *Spitzer* ch1–ch2 colors for nearby late-T and Y dwarfs. Black points are all objects with $T_{\rm eff} < 600$ K and measured parallaxes taken from Kirkpatrick et al. (2019, their Table 8). The red dashed lines in the left panel encompass the 1σ color range for CW1446. Overplotted in blue is the polynomial relation presented in Kirkpatrick et al. (2019). The four objects redder than CW1446 are *WISE* J220905.73 +271143.9 (labeled W2209 on the plot; Kirkpatrick et al. 2011), WISEA J235402.79+024014.1 (W2354; Schneider et al. 2015), *WISE* J035000.32–565830.2 (W0350; Kirkpatrick et al. 2012), and *WISE* J085510.83–071442.5 (W0855; Luhman 2014).

Gaia DR2 with full five-parameter solutions. These *Gaia* objects were placed at their expected positions at the time of the *WISE* observations so that, again, astrometry could be re-registered onto the absolute *Gaia* DR2 reference frame. Additional information on this process can be found in M19. These unWISE data were then associated with the position of the Earth at the mean time of each unWISE epoch, and an astrometric fit was run using the prescription discussed in Section 5.2.3 of Kirkpatrick et al. (2019).

The resulting fit is given in Table 1 and illustrated in Figure 2. The parallactic solution should be considered preliminary and of low confidence because there is only a single high-quality data point anchoring each side of the

parallactic ellipse. The low confidence of the solution is also reflected in the large parallactic error of ~15%.

5. Analysis

With a ch1–ch2 color of 2.986 ± 0.048, and a distance of $10.1^{+1.7}_{-1.3}$ pc, CW1446 is the one of the reddest, least luminous, and therefore likely coldest brown dwarfs known in the solar neighborhood. Figure 3 shows $T_{\rm eff}$ and $M_{\rm ch2}$ as a function of *Spitzer* ch1–ch2 color for a sample of known late-T and Y dwarfs from the literature (see Kirkpatrick et al. 2019, and references therein). The ch1–ch2 to $T_{\rm eff}$ and $M_{\rm ch2}$ to $T_{\rm eff}$ polynomial relations presented in Kirkpatrick et al. (2019)

imply a $T_{\rm eff}$ in the range $\sim$310–360 K for CW1446 (see Figure 3).

For such a cold $T_{\rm eff}$, and if we assume that CW1446 is a field object (i.e., with age in the $\sim$500 Myr–13 Gyr range), the BT-Settl models (Allard et al. 2012, 2013) imply a mass in the range 2–20 $M_{\rm Jup}$. However, given its relatively high tangential velocity ($59.7 \pm 9.0\ {\rm km\ s^{-1}}$), CW1446 is unlikely to be very young. If we assume that CW1446 is coeval with the population of nearby ultracool dwarfs, whose age is in the range $\sim$1.5–6.5 Gyr (see e.g., Wang et al. 2018, and references therein), we find its mass to be between 4 and 14 $M_{\rm Jup}$.

Despite being slightly bluer, our preliminary parallax suggests that CW1446 is as luminous as *WISE* J035000.32–565830.2, currently the second reddest brown dwarf known (ch1–ch2 $= 3.25 \pm 0.10$ mag, $M_{\rm ch2} = 15.90 \pm 0.04$ mag). Comparison to the Y0 dwarf spectral standard, *WISE* J173835.53+273259.0 (Cushing et al. 2011), shows that CW1446 is clearly redder (ch1–ch2 $= 02.986 \pm 0.048$ mag versus 2.620 ± 0.056 mag) and less luminous ($M_{\rm ch2} = 15.90 \pm 0.04$ mag versus 15.06 ± 0.04 mag). Interpolating the spectral type to *Spitzer* color and $M_{\rm ch2}$ relations presented in Kirkpatrick et al. (2019), we find that CW1446 would have a spectral type of $\approx$Y1.5. However, we warn the reader that the scatter in the spectral type to color and magnitude relations for such cold objects is still not well quantified or understood, with spectroscopically classified Y0 dwarfs occupying a $\sim$1 mag range in ch1–ch2 and a $\sim$1.3 mag range in $M_{\rm ch2}$ (see Figures 4 and 5 in Kirkpatrick et al. 2019). Moreover, the *Spitzer* ch1 and ch2 photometry probes a different wavelength regime than the near-infrared spectral types, which are defined based on the morphology of the J- and H-band spectra (Cushing et al. 2011), and are therefore likely sensitive to different physical and chemical processes. Therefore, further interpretation of CW1446 with respect to the rest of the cold brown dwarf population based on *Spitzer* data alone is unwarranted.

Shorter wavelength photometric detections are unavailable for this object, given that it is well below the detection threshold for existing optical and near-infrared surveys. Our dedicated FLAMINGOS-2 observations lead to MKO $J > 22.36$ mag (M19), implying $J - {\rm ch2} > 6.44$ mag, consistent with the $T_{\rm eff}$ derived here.

6. Discussion

The upcoming *Spitzer* astrometric observations will allow us to improve the constraint on the distance to this object, securing one of the two vertices of the parallactic ellipse. However, due to the end of the *Spitzer* mission, no further measurement is possible at the opposite vertex, limiting the improvement that we can expect. Further characterization of CW1446 anyway requires spectroscopic follow-up. Given the $T_{\rm eff}$ estimate and preliminary distance measurement presented here, the expected *H* magnitude for CW1446 is 24–25.5 mag, a depth prohibitive for ground-based spectroscopy with existing facilities. Therefore, spectroscopic characterization can only be provided by the upcoming *James Webb Space Telescope*.

CW1446 occupies the sparsely populated 300–400 K regime. W0855, however, remains the only $T_{\rm eff} < 300$ K object known to date. Given the brightness and proximity of W0855, Wright et al. (2014) estimated that the existing *WISE* data should contain of order 4–35 "W0855-like" objects, and predicted that, if such objects did indeed exist, astrometric

analysis of the combination of AllWISE and NEOWISE data would allow their discovery.

Yet W0855-like objects remain elusive, despite investigations of *WISE* and NEOWISE data using the CatWISE Preliminary Catalog (Eisenhardt et al. 2019) and the "Backyard Worlds: Planet 9" citizen science project (Kuchner et al. 2017).

The upcoming CatWISE 2020 catalog will be based on the full set of publicly available *WISE* and NEOWISE data covering the 2010–2018 baseline, and achieves significantly better completeness and motion sensitivity, so may reveal colder objects. Further advancement on the question of whether there is a low-mass cutoff to star formation may need to wait for the Near Earth Object Surveyor (formerly NEOCam), which will provide even deeper imaging of most of the sky at wavelengths similar to *W2*, with a mission length of at least 5 years.

ORCID iDs

Federico Marocco ⬤ https://orcid.org/0000-0001-7519-1700
J. Davy Kirkpatrick ⬤ https://orcid.org/0000-0003-4269-260X
Aaron M. Meisner ⬤ https://orcid.org/0000-0002-1125-7384
Dan Caselden ⬤ https://orcid.org/0000-0001-7896-5791
Michael C. Cushing ⬤ https://orcid.org/0000-0001-7780-3352
Jacqueline K. Faherty ⬤ https://orcid.org/0000-0001-6251-0573
Edward L. Wright ⬤ https://orcid.org/0000-0001-5058-1593

References

Allard, F., Homeier, D., & Freytag, B. 2013, MmSAI, 84, 1053
Allard, F., Homeier, D., Freytag, B., & Sharp, C. M. 2012, EAS, 57, 3
Caselden, D., Westin, P., III, Meisner, A., Kuchner, M., & Colin, G. 2018, WiseView: Visualizing motion and variability of faint WISE sources, Astrophysics Source Code Library, ascl:1806.004
Chen, T., & Guestrin, C. 2016, in Proc. 22nd ACM SIGKDD Int. Conf. on Knowledge Discovery and Data Mining, KDD '16, ed. B. Krishnapuram et al. (New York: ACM), 785
Cushing, M. C., Kirkpatrick, J. D., Gelino, C. R., et al. 2011, ApJ, 743, 50
Eisenhardt, P. R. M., Marocco, F., Fowler, J. W., et al. 2019, arXiv:1908.08902
Esplin, T. L., & Luhman, K. L. 2019, AJ, 158, 54

Faherty, J. K., Riedel, A. R., Cruz, K. L., et al. 2016, ApJS, 225, 10
Kirkpatrick, J. D., Cushing, M. C., Gelino, C. R., et al. 2011, ApJS, 197, 19
Kirkpatrick, J. D., Gelino, C. R., Cushing, M. C., et al. 2012, ApJ, 753, 156
Kirkpatrick, J. D., Martin, E. C., Smart, R. L., et al. 2019, ApJS, 240, 19
Kuchner, M. J., Faherty, J. K., Schneider, A. C., et al. 2017, ApJL, 841, L19
Lodieu, N., Zapatero Osorio, M. R., Béjar, V. J. S., & Peña Ramírez, K. 2018, MNRAS, 473, 2020
Luhman, K. L. 2014, ApJL, 786, L18
Luhman, K. L., Herrmann, K. A., Mamajek, E. E., Esplin, T. L., & Pecaut, M. J. 2018, AJ, 156, 76
Makovoz, D., & Khan, I. 2005, in ASP Conf. Ser. 347, Mosaicking with MOPEX, ed. P. Shopbell, M. Britton, & R. Ebert (San Francisco, CA: ASP), 81

Makovoz, D., & Marleau, F. R. 2005, PASP, 117, 1113
Marocco, F., Caselden, D., Meisner, A. M., et al. 2019, ApJ, 881, 17
Meisner, A. M., Caselden, D., Kirkpatrick, J. D., et al. 2019a, arXiv:1911.12372
Meisner, A. M., Lang, D., Schlafly, E. F., & Schlegel, D. J. 2019b, PASP, 131, 124504
Schlafly, E. F., Green, G. M., Lang, D., et al. 2018, ApJS, 234, 39
Schlafly, E. F., Meisner, A. M., & Green, G. M. 2019, ApJS, 240, 30
Schneider, A. C., Cushing, M. C., Kirkpatrick, J. D., et al. 2015, ApJ, 804, 92
Wang, Y., Smart, R. L., Shao, Z., et al. 2018, PASP, 130, 064402
Wright, E. L., Mainzer, A., Kirkpatrick, J. D., et al. 2014, AJ, 148, 82
Zapatero Osorio, M. R., Béjar, V. J. S., & Peña Ramírez, K. 2017, ApJ, 842, 65